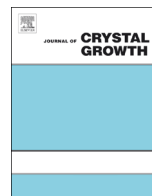




ELSEVIER

Contents lists available at ScienceDirect

Journal of Crystal Growth

journal homepage: www.elsevier.com/locate/jcrysgr

Growth of ultra-long sodium tungsten oxide and tungsten oxide nanowires: Effects of impurity and residue deposition



Tao Sheng^a, Padmanabha P. Chavvakula^b, Baobao Cao^{b,c}, Naili Yue^d,
Yong Zhang^d, Haitao Zhang^{b,*}

^a Optical Science and Engineering Program, The University of North Carolina at Charlotte, 9201 University City Boulevard, Charlotte, NC 28223, USA

^b Department of Mechanical Engineering and Engineering Science, The University of North Carolina at Charlotte, 9201 University City Boulevard, Charlotte, NC 28223, USA

^c School of Materials Science and Engineering, Southwest Jiaotong University, No. 111, 1st North Section, 2nd Ring Road, Chengdu, Sichuan 610031, PR China

^d Department of Electrical and Computer Engineering, The University of North Carolina at Charlotte, 9201 University City Boulevard, Charlotte, NC 28223, USA

ARTICLE INFO

Article history:

Received 16 October 2013

Received in revised form

21 January 2014

Accepted 8 March 2014

Communicated by J.M. Redwing

Available online 18 March 2014

Keywords:

A1. Nanostructures

A2. Growth from vapor

A3. Chemical vapor deposition processes

B1 Tungstates

B1. Nanomaterials

ABSTRACT

Ultra-long nanowires of sodium tungsten oxide and tungsten oxide were synthesized by simply heating tungsten source under a low oxygen pressure environment. The nanowires have diameters of ~40 to 500 nm and lengths from tens to several hundred microns. The majority of the nanowires were found to be triclinic Na₅W₁₄O₄₄ with small amount of monoclinic WO₃. Triclinic Na₂W₄O₁₃ microplates with a rectangular shape grown together with the nanowires were also identified. The formation of ultra-long nanowires is explained by the vapor–solid (VS) growth mechanism. Effects of impurity and residue deposition have been thoroughly investigated. With a low concentration even smaller than 10 ppm (parts per million), the sodium impurity in the tungsten source could result in the formation of sodium tungsten phases. The growth of nanowires could be enhanced with the presence of residue deposition and the enhancement was attributed to the production of local vapor pressure from the residue deposition.

© 2014 Elsevier B.V. All rights reserved.

1. Introduction

Tungsten trioxide (WO₃) is a versatile semiconductor material with a wide range of applications [1], such as smart devices (e.g., electrochromic [2], photochromic [3], and gasochromic devices [4]), solar water splitting [5], gas sensors [6], memory devices [7], filed emission [8], and photodetectors [9], etc. At room temperature, the most stable phase is the monoclinic γ -WO₃ which has a tilted ReO₃-type crystal structure with corner-sharing WO₆ octahedra [10,11]. Light ions, such as H⁺, Li⁺, and Na⁺ can be easily intercalated into the WO₃-framework forming a family of different metal tungsten oxides (i.e. tungstates or tungsten bronzes) with a general formula of M_x^(z)WO_{3-y+zx/2}, where M is the bronze-forming metal, z the valency of M, and y characterizes oxygen deficiency with $y \neq zx/2$ [12]. Among them, sodium tungsten oxides (Na_xWO_{3-y+x/2}) are one group of tungsten bronzes which have been extensively studied due to their unique character of tuning material structures and properties by composition control. For example, the Na_xWO₃

bronzes ($0 < x < 1$), formed by doping the insulating WO₃ host with Na ions, can change from n-type semiconductor ($x < 0.3$) to metallic conductor ($x > 0.3$) by increasing the x value [12,13]. Attractive two-dimensional high-temperature superconductivity of Na-doped WO₃ has also been observed with a surface composition of Na_xWO₃ ($x=0.05-0.07$) [13–15]. With the increase of x, the Na_xWO₃ can have a continuous color change from blue to violet, red, and golden, as well as a crystal structure change from monoclinic through orthorhombic, tetragonal, to cubic [16]. Sodium tungsten oxides have wide applications in photocatalysis [17], chemical analysis [18], fuel cells [19], smart windows [20], and near-infrared shielding [21].

Recent years, with the advancement of nanoscale research, nanostructured WO₃ especially the one-dimensional (1D) nanostructures (e.g., nanowires, nanobelts, and nanorods, etc.) have attracted intensive research efforts on material synthesis, property measurement, and device testing [22]. However, the study of 1D sodium tungsten oxide nanostructures is limited so far with only a few papers published on cubic Na_xWO₃ nanorods and nanobelts [23], hexagonal Na_{0.17}WO_{3.085}·0.17H₂O and Na_{0.3}WO₃ nanorods [21], Na₂W₄O₁₃ nanofibers [24], cubic and tetragonal Na_xWO₃ nanobundles [25], and triclinic Na_{0.5}WO_{3.25} nanoplates [26].

* Corresponding author. Tel.: +1 704 687 8128.

E-mail address: h Zhang@unc.edu (H. Zhang).

In this work, we report the growth of ultra-long nanowires of sodium tungsten oxide and tungsten oxide with diameters of ~ 40 to 500 nm and lengths from tens to several hundred microns by simply heating tungsten source under low pressure oxygen environment. The majority of the nanowires were found to be triclinic $\text{Na}_5\text{W}_{14}\text{O}_{44}$ with small amount of monoclinic WO_3 . Rectangular microplates of triclinic $\text{Na}_2\text{W}_4\text{O}_{13}$ grown together with the nanowires were also identified. It was observed that the formation of nanowires could be enhanced with the presence of residue deposition on the wall of reaction chamber. The growth mechanism of the ultra-long nanowires will be discussed. The impurity effect on the formation of sodium tungsten phases and the effect of residue deposition on the enhanced nanowire growth have been thoroughly investigated.

2. Experimental details

Samples were synthesized using a chemical vapor deposition (CVD) method. A home-built hot-wall low pressure CVD system with a reaction chamber of 1" diameter quartz tube heated by two semi-cylindrical ceramic fiber heaters was employed for the growth. Similar CVD systems have been used for the growth of nanostructures of boron [27], borides [28], titanium oxide [29], and tungsten oxide [30]. Silicon (100) substrates with a $1\text{-}\mu\text{m}$ -thick thermally grown oxide layer ($\text{SiO}_2\text{-Si}$, University Wafer) were used in this study. Substrates were first cut into rectangular pieces with a size of $10\text{ mm} \times 35\text{ mm}$, and then were ultrasonically cleaned with acetone and alcohol for about 10 min each followed by blow-drying with nitrogen gas. Tungsten powders with a purity of 99.9% (Alfa Aesar 39749, Lot #: H17Q06, -325 mesh) were mainly used as the source materials for the growth. Other tungsten sources with different purities and sizes were also used for control experiments. In a typical experiment, about 2 g tungsten powders were loaded into a quartz boat at its upstream end with a substrate located about 63 mm apart at the downstream end. The boat was then loaded inside the reaction chamber with the tungsten source located at the center of the furnace. The reaction chamber was first pumped down to an ultimate vacuum pressure of ~ 7 mTorr, and then brought up to 110 mTorr

with 1 sccm (standard cubic centimeter per minute) O_2 and 10 sccm Ar. The system was then ramped to a heating temperature of 1000°C at the center in 30 min and held for 4 h, followed by cooling down to room temperature in about 5 h. Variations of nanostructure morphologies were observed if multiple growths were employed repeatedly in the same reaction chamber of quartz tube. Hence, a series of experiments were performed in the same reaction chamber with the increase of the growth number (defined as the order of the growths employed in the same reaction chamber).

The morphology and composition of the as-synthesized samples were analyzed by scanning electron microscopy (SEM, JEOL JSM-6480) and energy dispersive X-ray spectroscopy (EDS, Oxford Instrument INCA). Crystal structures were characterized using X-ray diffraction (XRD, PANXpert X'pert Pro MRD with $\text{Cu } K_\alpha$ radiation at $\lambda = 1.5418 \text{ \AA}$) and transmission electron microscopy (TEM, JEOL JEM-2100 LaB₆ operated at an accelerating voltage of 200 kV). Micro-Raman spectroscopy (Horiba Scientific, Jobin Yvon Labram HR800 with 532 nm excitation laser) was performed to confirm the phases of different nanostructures.

3. Results and discussion

3.1. Morphology and structure characterization

Fig. 1(a) shows SEM images of typical morphologies of the as-synthesized nanostructures grown on a $\text{SiO}_2\text{-Si}$ substrate. The nanostructures are ultra-long nanowires with lengths from tens of microns up to several hundred microns and diameters about $40\text{--}500$ nm. The deposition of nanowires was generally located on the substrates with a growth temperature range from 660 to 420°C . Close-up observations at high magnification revealed that some nanowires were cylinder-shaped and some were belt-shaped (shown in the inset of Fig. 1(a)). At some locations, microplate structures with a regular rectangular shape were grown among the nanowires as demonstrated in Fig. 1(b) and its inset. The chemical compositions of these structures were identified by EDS. A representative EDS spectrum in Fig. 1(c) shows the existence of W, Na, O, and Si signals in the specimen, where

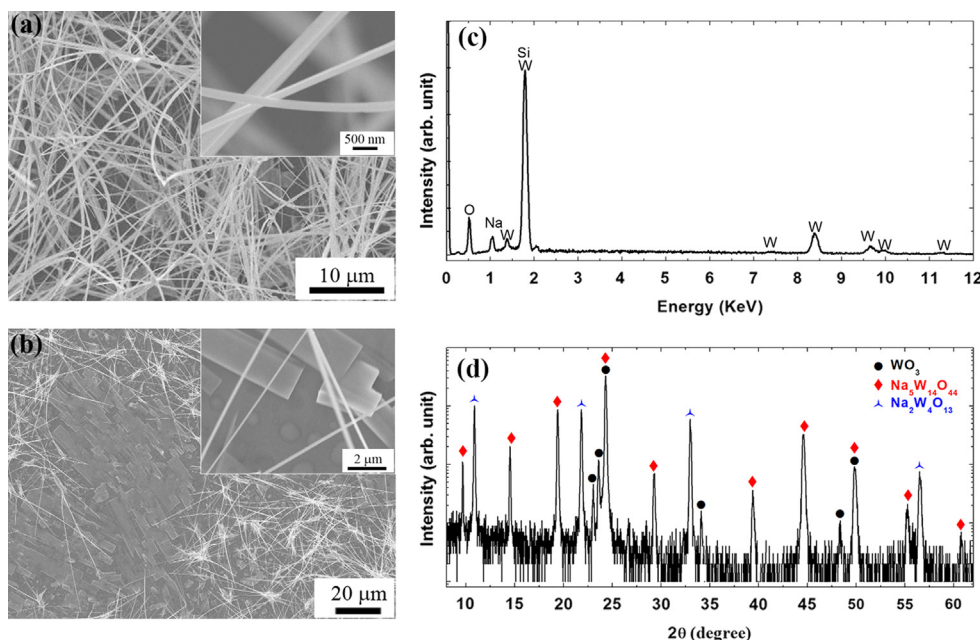


Fig. 1. SEM images of (a) dense array of the as-synthesized ultra-long nanowires on $\text{SiO}_2\text{-Si}$ substrate and (b) the rectangular microplates grown among the nanowires. The insets show corresponding close-up views. (c) EDS and (d) XRD spectra showing the chemical compositions and phases of the deposition.

the Si signal was expected from the substrate and O was partially from the substrate. The crystal structures of the as-synthesized specimens were examined using XRD. The diffraction peaks were carefully indexed and the deposition was identified as two phases of sodium tungsten oxides and one phase of tungsten oxide as indicated on Fig. 1(d). The two sodium tungsten oxide phases are the triclinic $\text{Na}_5\text{W}_{14}\text{O}_{44}$ phase (ICDD PDF 04-012-4449, $a=7.2740 \text{ \AA}$, $b=7.2911 \text{ \AA}$, $c=18.5510 \text{ \AA}$, $\alpha=96.3750^\circ$, $\beta=90.8920^\circ$, $\gamma=119.6560^\circ$) and the triclinic $\text{Na}_2\text{W}_4\text{O}_{13}$ phase (ICDD PDF 04-012-7108, $a=11.1630 \text{ \AA}$, $b=3.8940 \text{ \AA}$, $c=8.2550 \text{ \AA}$, $\alpha=90.60^\circ$, $\beta=131.36^\circ$, $\gamma=79.70^\circ$). The tungsten oxide phase is the monoclinic WO_3 phase (ICDD PDF 01-083-0950, $a=7.30084 \text{ \AA}$, $b=7.53889 \text{ \AA}$, $c=7.6896 \text{ \AA}$, $\beta=90.8920^\circ$). Detailed peak indices for each phase are listed in Table S1 in Supplementary material.

The XRD measurements revealed the overall structure information of the deposition on the substrates. To obtain detailed information on the crystallinity, composition, and growth direction of different structures, TEM analyses with imaging, electron diffraction, and EDS were performed on more than 20 nanowires. The majority of the nanowires were identified as the triclinic $\text{Na}_5\text{W}_{14}\text{O}_{44}$ (shown in Fig. 2(a)–(c)). Fig. 2(a) shows a low magnification TEM image of a portion of an ultra-long nanowire. Close-up analyses of the section indicated by the rectangle were performed with high-resolution TEM (HRTEM) imaging and selective area electron diffraction (SAED). The HRTEM image in Fig. 2(b) demonstrates that the nanowire has a single-crystalline structure. The corresponding diffraction pattern in the inset of Fig. 2(b) was recorded in $[\bar{1}10]$ axis. Based on the analyses on a series of diffraction patterns and HRTEM images, the nanowire was

confirmed as the triclinic $\text{Na}_5\text{W}_{14}\text{O}_{44}$. The growth direction of the $\text{Na}_5\text{W}_{14}\text{O}_{44}$ nanowire was determined to be parallel to the (001) plane which has a d-spacing of $\sim 1.8 \text{ nm}$. The chemical composition of the nanowire was revealed by EDS. Fig. 2(c) shows the nanowire consisted of W, Na, and O and no other impurities were detected. (Note: the Cu and C signals came from the supporting Cu grid with lacey carbon and the Cr signal from the tip of JEOL double tilt holder. They were not compositions from the nanowires and other structures studied here.) Only small amount of nanowires were found as the monoclinic WO_3 (Fig. 2(d)–(f)). The SAED shown in the inset of Fig. 2(e) was recorded in $[100]$ zone. The growth direction of the WO_3 nanowire was determined to be perpendicular to the (002) plane with a d-spacing of $\sim 0.38 \text{ nm}$. EDS spectrum in Fig. 2(f) shows the nanowire consisted of W and O without Na or other impurities being detected. Both the $\text{Na}_5\text{W}_{14}\text{O}_{44}$ and the WO_3 phases are coincident with the phases found in XRD measurements, confirming the ultra-long nanowires are mainly $\text{Na}_5\text{W}_{14}\text{O}_{44}$ phase with small amount of WO_3 phase. However, the $\text{Na}_2\text{W}_4\text{O}_{13}$ phase appeared in the XRD results was not found with any nanowires in the TEM analyses. Hence, the rectangular microplate structures shown in Fig. 1(b) were specifically collected for TEM examination. These microplate structures were identified to be the triclinic $\text{Na}_2\text{W}_4\text{O}_{13}$ phase (Fig. 2(g)–(i)). The SAED in Fig. 2(h) was recorded in $[101]$ axis. No high-quality HRTEM images were acquired for the $\text{Na}_2\text{W}_4\text{O}_{13}$ plate due to its large thickness. The long edge of the plate was identified as parallel to the (010) plane and the short edge parallel to the $(\bar{1}01)$ plane. As shown in SEM images (Fig. 1(b) and inset), the $\text{Na}_2\text{W}_4\text{O}_{13}$ microplates were grown with the plate surface

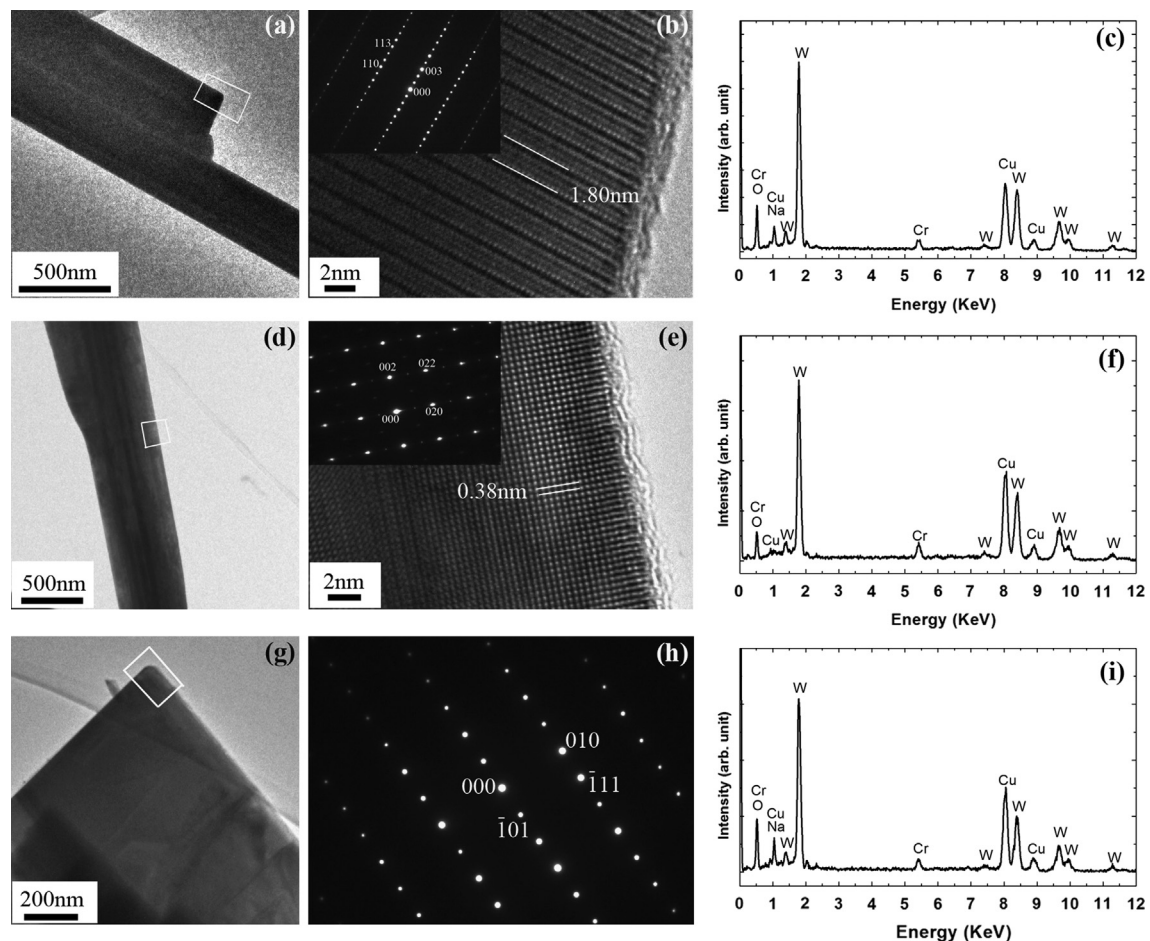


Fig. 2. TEM images at low-magnification, HRTEM images/SAED patterns, and EDS spectra of a $\text{Na}_5\text{W}_{14}\text{O}_{44}$ nanowire (a)–(c), a WO_3 nanowire (d)–(f), and a $\text{Na}_2\text{W}_4\text{O}_{13}$ microplate (g)–(i). Note: no HRTEM image for $\text{Na}_2\text{W}_4\text{O}_{13}$ plate due to its large thickness.

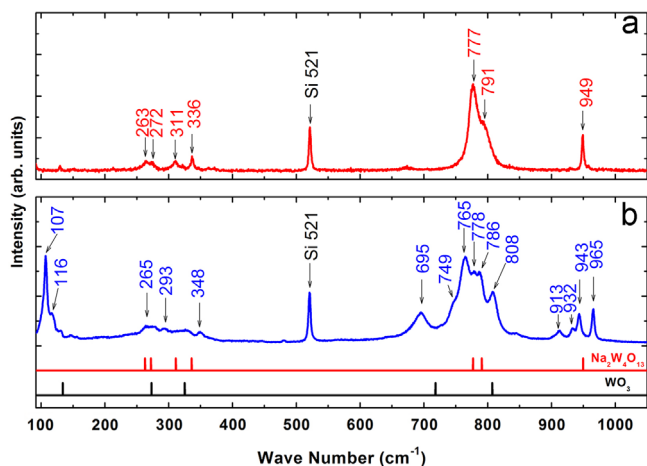


Fig. 3. Micro-Raman spectra of (a) the microplates matching the reported peak positions of the $\text{Na}_2\text{W}_4\text{O}_{13}$ phase, and (b) the nanowires with comparisons to the reported major peak positions of $\text{Na}_2\text{W}_4\text{O}_{13}$ (red line) and WO_3 (black line) phases. (For interpretation of the references to color in this figure legend, the reader is referred to the web version of this article.)

parallel to the substrate surface, while only (100), (200), and (300) series of peaks of $\text{Na}_2\text{W}_4\text{O}_{13}$ were shown in the XRD spectra (Table S1 in Supplementary material). This result indicates the microplate surface is the (100) surface consistent with the cleavage plane of $\text{Na}_2\text{W}_4\text{O}_{13}$ [31]. Hence, the long edge of $\text{Na}_2\text{W}_4\text{O}_{13}$ plate can be figured out as the \vec{c} axis ([001]) and the short edge is along the \vec{b} axis ([010]). Fig. 2(i) shows the plate structure also consisted of W, Na, and O and no other impurities were detected. Normalized to the highest W peak, the Na peak intensity in Fig. 2(i) is higher than the one in Fig. 2(c). This result indicates a higher Na:W ratio for the $\text{Na}_2\text{W}_4\text{O}_{13}$ plate structure than the one for $\text{Na}_5\text{W}_{14}\text{O}_{44}$ nanowires and this is consistent with the compositions of these two phases.

Micro-Raman spectroscopy was also carried out at room temperature in ambient atmosphere to confirm the phases of the microplates and ultra-long nanowires. Fig. 3(a) shows the Micro-Raman spectrum of the microplates. The Raman lines at 949, 794–777, and 366–263 cm^{-1} closely match the reported $\text{Na}_2\text{W}_4\text{O}_{13}$ Raman shift frequencies at 953, 790–774, and 336–265 cm^{-1} , respectively [32]. (Note: the peak at 521 cm^{-1} is for Si from the substrate.) The Raman spectrum from the ultra-long nanowires is shown in Fig. 3(b). The spectrum shows major peaks in 100–150 cm^{-1} , 650–900 cm^{-1} , and 900–1000 cm^{-1} regions. As compared to the reported peak positions (shown by solid lines in Fig. 3(b)), the nanowires consist of only a little amount of or no WO_3 [10] and $\text{Na}_2\text{W}_4\text{O}_{13}$ phases [32]. Major peaks at 107, 695, 765, 913, 943, and 965 cm^{-1} do not match the Raman features reported in the literature. According to the TEM results, the nanowires are mainly $\text{Na}_5\text{W}_{14}\text{O}_{44}$, therefore these peaks should belong to the $\text{Na}_5\text{W}_{14}\text{O}_{44}$ phase. Since no Raman spectrum has been reported so far for the $\text{Na}_5\text{W}_{14}\text{O}_{44}$ phase, this study reports the first Raman spectrum for $\text{Na}_5\text{W}_{14}\text{O}_{44}$ which requires further investigation on pure $\text{Na}_5\text{W}_{14}\text{O}_{44}$ materials to get detailed structure information.

3.2. Impurity effect

No catalysts were employed for the deposition of the nanowires and no catalyst particles were found along the nanowires examined by electron microscopies. Hence, catalyst-assisted growth mechanisms can be ruled out for the nanowire growth reported here. The nanowires were grown via a non-catalyst vapor–solid (VS) process in which the vapors produced by heating the source material were transported to the growth area

downstream with lower temperature forming deposition. The formation mechanism can be explained by the suppressed two-dimensional nucleation on side faces resulting from the low vapor supersaturation at the growth temperature [33]. Based on the compositional analyses, it is important to first figure out where the Na came from. Heated at elevated temperatures, the W source, quartz tube, and quartz boat were the three possible sources for Na. The Na concentrations in the W source with 99.9% purity (Alfa Aesar 39749, Lot #: H17Q06), quartz tube (QSI Quartz Scientific), and quartz boat (GE 214 quartz, Wilmad Labglass) were 20 ppm (parts per million), 1 ppm, and 0.7 ppm respectively [34]. To identify the major source(s) of the Na contents, control experiments were employed by using W source with higher purities of 99.995% (Materion T-2049, with 0.065 ppm Na) and 99.999% (Materion T-2023, with 0.05 ppm Na) as other growth parameters kept the same. These ultra-high purity W sources produced pure tungsten oxide deposition. No Na content was detected beyond the detection limit of the EDS system. These results verified the Na contents were mainly from the W source with 99.9% purity, not from the quartz tube and boat. Another batch of the 99.9% purity W source (Lot#: G07×064) with the Na contents smaller than 10 ppm was also used in growth. However, the deposition was still dominated by sodium tungsten oxide phases with small amount of tungsten oxide.

A question then arises: why the Na contents in the W sources at such low concentrations could affect the growth so significantly in our experiments? Growth of tungsten oxide 1D nanostructures using similar thermal evaporation with tungsten powders has been reported and no impurity effect of Na was found [6,35,36]. Although detailed composition information is not available from these reports, this question can be explained by the differences in the supply of tungsten oxide vapors in different experiments. Tungsten has an extremely low vapor pressure below 10^{-11} Torr even at a high heating temperature of 2000 °C [37], so in all growths tungsten vapor directly from the thermal evaporation of W source was negligible and the depositions were formed from tungsten oxide vapors. In the previous reports [6,35,36], the tungsten powders were all heated at high vacuum pressures with high O_2 partial pressures. Large amount of tungsten oxide vapors were produced resulting from the high oxidation rate of the tungsten sources. Therefore, the impurity effect on the growth of nanostructures in these reports was negligible if any Na impurities presented in the sources were at ppm levels. In our experiments, the W source was first slowly oxidized at 1000 °C with 1 sccm O_2 and the oxidized source was then evaporated producing WO_3 and other substoichiometric tungsten oxide vapors. The tungsten oxide vapors produced this way were limited by the slow oxidation as indicated by (1) only small amount of the tungsten source was consumed during the growth and (2) the tungsten source was only partially oxidized with a dark blue color on the top while the majority of the source was still kept as tungsten. Due to their low concentration, the exact compositions of the Na contents in the tungsten source are not clear. However, the evaporation rates of the Na contents are expected to be high as heated at 1000 °C. This assumption can be verified by two facts. First, no Na was detected on the substrate with growth temperature higher than 850 °C showing high evaporation rates of the Na contents at temperature higher than 850 °C. Second, no Na was found in the deposition along the whole substrate in the control experiments using the used 99.9% purity W source. This result indicates that the majority of Na contents were already evaporated during the previous experiment. Hence, despite the low concentration of Na contents in the source, the total amount of Na-based vapors produced during the growth was comparable to or more than the amount of tungsten oxide vapors and resulted in the dominating deposition of sodium tungsten oxide phases in the nanowire growth area. It is

worth mentioning that a thick coating was formed with little nanowires when the ultra-high purity W sources and the used 99.9% purity W source were used. The varnishing of $\text{Na}_5\text{W}_{14}\text{O}_{44}$ nanowires was apparently due to the reduction of Na contents in the sources. The disappearance of WO_3 nanowires, however, was attributable to the high deposition rate resulting from the enhanced source oxidation process. After the deposition, the ultra-high purity W sources and the used 99.9% purity W source all turned into greenish yellow, the characteristic color of WO_3 , showing enhanced oxidation process of the tungsten sources. The oxidation process was enhanced because the used W source was already partially oxidized and the ultra-high purity W sources had very small particle sizes (i.e., large surface-to-volume ratios) for easy oxidation (see size information in Table S2 in Supplementary material). The above discussion reveals the extreme sensitivities of the nanostructure composition on the purity of source materials and the thermal properties of impurities. Thus, special care must be taken to achieve composition controls for the growth of different nanostructures.

3.3. Enhanced nanowire growth by residue deposition

As shown by the photograph in Fig. 4(a), for a series of growths performed in the same reaction chamber, the morphology of the nanowires changed with the increase of the growth number. Three growth zones of nanowires can be identified based on the coverage and density of the nanowires as shown in Fig. 4(a) by the labeled regions with a bright gray color. The growth Zone I was located at high temperature end ranging from 660 to 520 °C, Zone II was from 520 to 470 °C, and Zone III from 470 to 420 °C. Detailed morphological changes are demonstrated in Fig. 5 with SEM images. For the first growth (Fig. 5(a)–(c)) in a new clean reaction chamber, there were only a little nanowires scattered in Zone I (Fig. 5(a)), ultra-long nanowires were mostly found in Zone II with higher density and coverage (Fig. 5(b)), and in Zone III the coverage, density, and length of nanowires gradually reduced as the growth location moved downstream (Fig. 5(c)). With the growth number increased to the third growth (Fig. 5(d)–(f)) and to the fifth growth (Fig. 5(g)–(i)), the coverage, density, and length of the nanowires increased in all three zones. Zone I had the most significant morphology changes as shown by Figs. 4(a) and 5(g). After the fifth growth in the same reaction chamber, the deposition of ultra-long nanowires almost covered all three zones. For Zones I and II, no significant morphology changes were observed with further increase of the growth number up to 8th growth. However, for Zone III the microplate structures (shown in inset of

Fig. 5(i)) kept increasing significantly with the growth number. EDS study revealed the change of Na concentration in the deposition with the growth number. Fig. 4(b) shows the change of the Na:W ratios with the increase of growth number at different nanowire growth zones. Generally, the Na:W ratios at all growth zones increased with the increase of growth number. The large fluctuation of the Na:W ratio at Zone III was mainly due to the uneven distribution of Na content with different morphologies at Zone III.

A mechanism of residue deposition enhanced growth was proposed to explain the morphology changes of the nanowires with the growth number. Since the CVD setup employed here was a hot-wall CVD system, deposition formed on the substrate surface as well as on the inner wall of the reaction chamber (i.e. the quartz tube) in the growth area. Residue deposition was found on the quartz tube which could be distinguished by the color change on the quartz tube after each growth. With the increase of the growth number for the same reaction chamber, the residue deposition on the inner wall of the tube also increased. If a clean quartz tube free of any residue deposition is employed as the reaction chamber, the vapors are supplied only from the source materials forming deposition in the growth area at growth temperature (as shown by the schematics in Fig. 6(a)). When a quartz tube with residue deposition from previous depositions is used repeatedly as the reaction chamber, the residue deposition heated at the growth temperature will also produce vapor locally. Therefore, the vapors from both the source materials and the local residue deposition will result in an enhanced growth of nanowires in the nanowire growth zones (Fig. 6(b)). To prove this hypothesis, control experiments were performed utilizing a quartz tube used multiple times previously (e.g., a growth number of 9). The experiments were carried out without any source materials while other growth parameters remained the same. Similar nanowires were found on the substrate in the nanowire growth zones. Without the source materials, the residue deposition from the tube surface was the only possible source that could produce vapors forming nanowires on the substrate (Fig. 6(c)). This result confirmed the nanowire growth could be enhanced by the presence of the residue deposition and explained the morphology changes of the nanowires with the increase of the growth number.

The general trend of Na:W ratios with the growth number can also be explained by the aforementioned effect of residue deposition. The sodium contents from the residue deposition would join the new Na contents from the W source forming deposition with higher Na:W ratios. Fig. 7 shows the XRD spectra of a series of specimens with the growth number increased from 1 to 5. The XRD

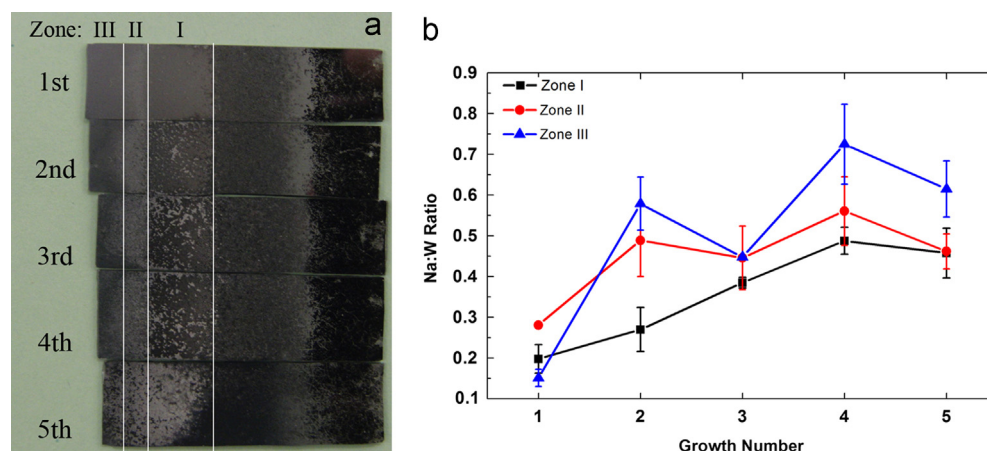


Fig. 4. (a) Photograph of a series of specimens grown in the same reaction chamber with the increase of growth number showing different growth zones and corresponding morphology changes. (b) Changes of Na:W ratios with the increase of growth number at different growth zones.

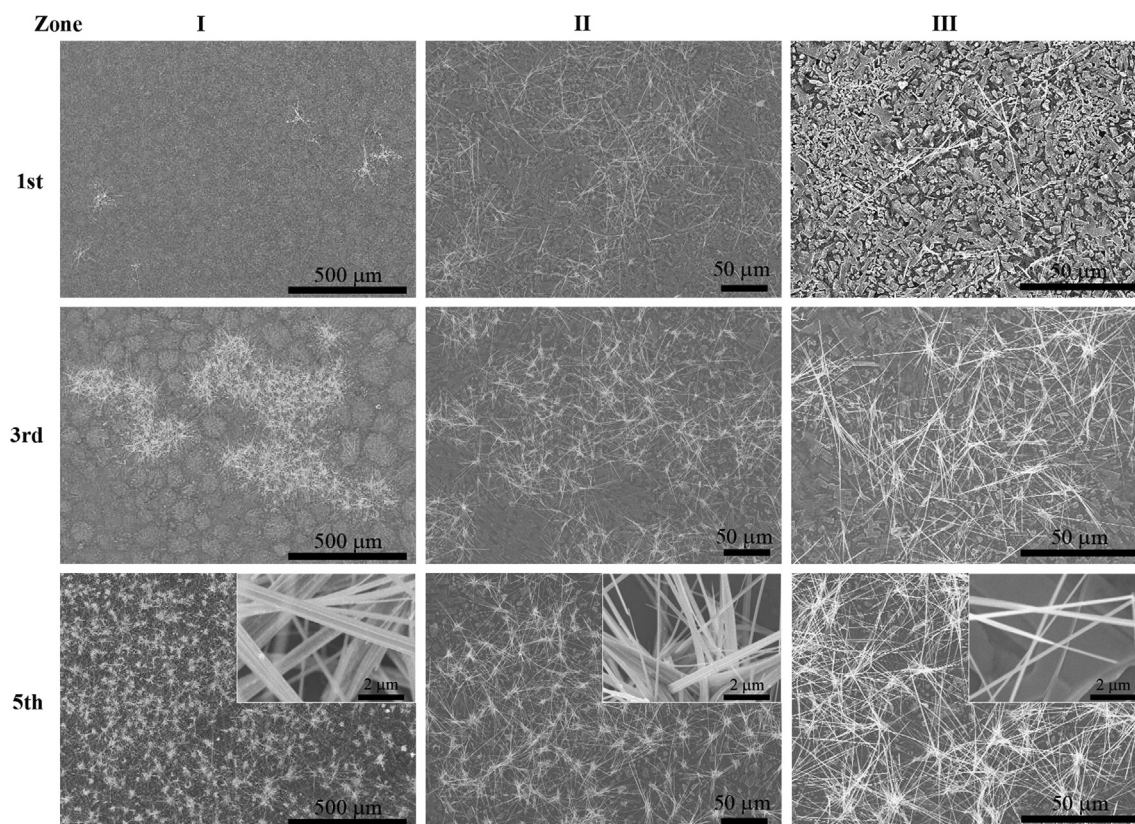


Fig. 5. Low magnification SEM images of the nanowires at different growth zones showing morphological changes with the increase of the growth number. The insets show detailed structures of the nanowires at high magnification.

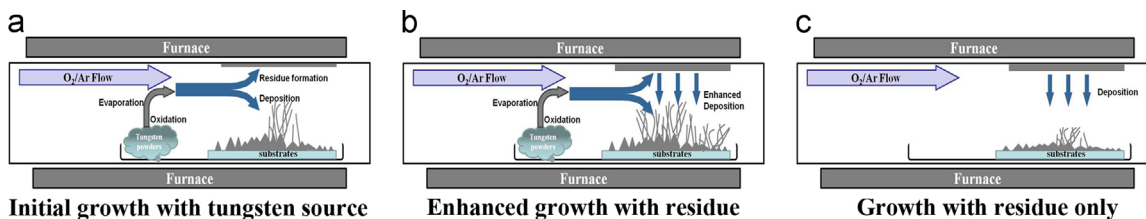


Fig. 6. Schematic drawings showing (a) growth with tungsten source in a new tube, (b) enhanced growth with both residue deposition and tungsten source, and (c) growth with residue deposition only.

spectra also reveal the revolution of the three phases with changes of relative concentrations as the growth number increased. Compared to the WO_3 phase, the $\text{Na}_5\text{W}_{14}\text{O}_{44}$ and the $\text{Na}_2\text{W}_4\text{O}_{13}$ phases increased significantly as the growth number increased from 1 to 5. And in the 5th growth, $\text{Na}_2\text{W}_4\text{O}_{13}$ became the dominated phase compared to the other two phases due to the increased formation of $\text{Na}_2\text{W}_4\text{O}_{13}$ microplates. These results are consistent with the SEM observation (Fig. 5) and the compositional changes from the EDS measurements (Fig. 4(b)).

4. Conclusions

In summary, the growth of ultra-long nanowires of triclinic $\text{Na}_5\text{W}_{14}\text{O}_{44}$ and monoclinic WO_3 was realized by simply heating the tungsten source under low oxygen pressure environment. The nanowires were ~ 40 to 500 nm in diameter and up to several hundred microns in length. The majority of the nanowires were $\text{Na}_5\text{W}_{14}\text{O}_{44}$ with a small amount of WO_3 . Triclinic $\text{Na}_2\text{W}_4\text{O}_{13}$ microplates with a rectangular shape were also found grown together with the nanowires. The growth mechanism of the ultra-long nanowires is explained by the VS process. The

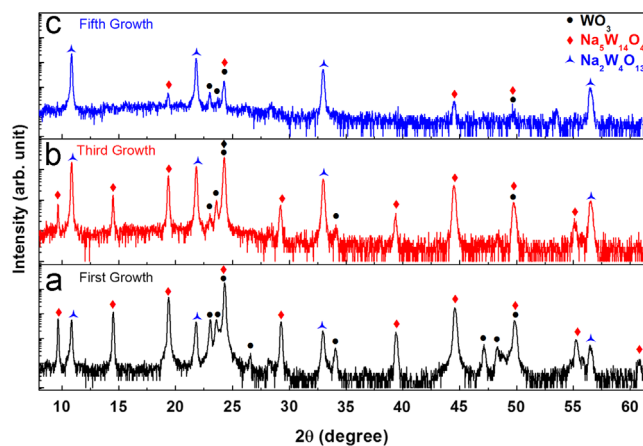


Fig. 7. XRD spectra of the as-synthesized specimen with the increase of growth number from 1 to 5.

composition and crystal structure of the as-synthesized samples have been fully characterized using SEM, EDS, TEM, and Micro-Raman. Effects of impurity and residue deposition have been

thoroughly investigated. The formation of sodium tungsten phases was attributed to the sodium impurity in the tungsten source even at a low concentration smaller than 10 ppm. This result shows the composition and structure of nanostructures were very sensitive on the purity of the source materials and the thermal properties of the impurities. With the presence of residue deposition, the nanowire growth could be enhanced and the enhancement was due to the production of local vapor pressure from the residue deposition. This discovery may be employed to facilitate large-scale growth of nanostructures.

Acknowledgments

This work was supported by the National Science Foundation (DMR-1006547), the start-up fund from the Department of Mechanical Engineering and Engineering Science (MEES) and Charlotte Research Institute at the University of North Carolina at Charlotte (UNC Charlotte), and the faculty research grant from UNC Charlotte. The authors appreciate the Department of MEES and the Center for Optoelectronics and Optical Communications at UNC Charlotte for the support of multiuser facilities.

Appendix A. Supplementary material

Supplementary data associated with this article can be found in the online version at <http://dx.doi.org/10.1016/j.jcrysgro.2014.03.013>.

References

- [1] S.K. Deb, Opportunities and challenges in science and technology of WO_3 for electrochromic and related applications, *Sol. Energy Mater. Sol. Cells* 92 (2008) 245–258.
- [2] J. Wang, E. Khoo, P.S. Lee, J. Ma, Synthesis, assembly, and electrochromic properties of uniform crystalline WO_3 nanorods, *J. Phys. Chem. C* 112 (2008) 14306–14312.
- [3] C. Bechinger, E. Wirth, P. Leiderer, Photochromic coloration of WO_3 with visible light, *Appl. Phys. Lett.* 68 (1996) 2834–2836.
- [4] H. Chen, N. Xu, S. Deng, D. Lu, Z. Li, J. Zhou, J. Chen, Gasochromic effect and relative mechanism of WO_3 nanowire films, *Nanotechnology* 18 (2007).
- [5] X. Liu, F. Wang, Q. Wang, Nanostructure-based WO_3 photoanodes for photoelectrochemical water splitting, *Phys. Chem. Chem. Phys.* 14 (2012) 7894–7911.
- [6] B. Cao, J. Chen, X. Tang, W. Zhou, Growth of monoclinic WO_3 nanowire array for highly sensitive NO_2 detection, *J. Mater. Chem.* 19 (2009) 2323–2327.
- [7] Y. Zhang, S.H. Lee, A. Mascarenhas, S.K. Deb, An UV photochromic memory effect in proton-based WO_3 electrochromic devices, *Appl. Phys. Lett.* 93 (2008).
- [8] J. Chen, Y.Y. Dai, J. Luo, Z.L. Li, S.Z. Deng, J.C. She, N.S. Xu, Field emission display device structure based on double-gate driving principle for achieving high brightness using a variety of field emission nanoemitters, *Appl. Phys. Lett.* 90 (2007).
- [9] L. Li, Y. Zhang, X. Fang, T. Zhai, M. Liao, X. Sun, Y. Koide, Y. Bando, D. Golberg, WO_3 nanowires on carbon papers: electronic transport, improved ultraviolet-light photodetectors and excellent field emitters, *J. Mater. Chem.* 21 (2011) 6525–6530.
- [10] M.F. Daniel, B. Desbat, J.C. Lassegues, B. Gerand, M. Figlarz, Infrared and Raman-study of WO_3 Tungsten Trioxides and $\text{WO}_3 \cdot x\text{H}_2\text{O}$ tungsten trioxide hydrates, *J. Solid State Chem.* 67 (1987) 235–247.
- [11] P. Roussel, P. Labbe, D. Groult, Symmetry and twins in the monophosphate tungsten bronze series $(\text{PO}_2)_4(\text{WO}_3)_m$ ($2 \leq m \leq 14$), *Acta Crystallogr. Sect. B-Struct. Sci.* 56 (2000) 377–391.
- [12] L. Bartha, A.B. Kiss, T. Szalay, Chemistry of tungsten-oxide bronzes, *Int. J. Refract. Met. Hard Mat.* 13 (1995) 77–91.
- [13] S. Reich, G. Leituss, Y. Tssaba, Y. Levi, A. Sharoni, O. Millo, Localized high-Tc superconductivity on the surface of Na-doped WO_3 , *J. Supercond.* 13 (2000) 855–861.
- [14] S. Reich, Y. Tssaba, Possible nucleation of a 2D superconducting phase on WO_3 single crystals surface doped with Na^+ , *Eur. Phys. J. B* 9 (1999) 1–4.
- [15] A. Shengelaya, S. Reich, Y. Tssaba, K.A. Muller, Electron spin resonance and magnetic susceptibility suggest superconductivity in Na doped WO_3 samples, *Eur. Phys. J. B* 12 (1999) 13–15.
- [16] J. Guo, C. Dong, L.H. Yang, G.C. Fu, A green route for microwave synthesis of sodium tungsten bronzes Na_xWO_3 ($0 < x < 1$), *J. Solid State Chem.* 178 (2005) 58–63.
- [17] A. Kudo, H. Kato, Photocatalytic activities of $\text{Na}_2\text{W}_4\text{O}_{13}$ with layered structure, *Chem. Lett.* (1997) 421–422.
- [18] M.A. Wechter, A.F. Voigt, H.R. Shanks, G. Carter, R. Guglielmi, G.M. Ebert, Use of metal tungsten bronze electrodes in chemical analysis, *Anal. Chem.* 44 (1972) 850–853.
- [19] L. Adjianto, R. Kuengas, J. Park, J.M. Vohs, R.J. Gorte, SOFC anodes based on infiltration of tungsten bronzes, *Int. J. Hydrog. Energy* 36 (2011) 15722–15730.
- [20] T. Gao, B.P. Jelle, Visible-light-driven photochromism of hexagonal sodium tungsten bronze nanorods, *J. Phys. Chem. C* 117 (2013) 13753–13761.
- [21] C. Guo, S. Yin, T. Sato, Synthesis of one-dimensional hexagonal sodium tungsten oxide and its near-infrared shielding property, *Nanosci. Nanotechnol. Lett.* 3 (2011) 413–416.
- [22] H. Zheng, J.Z. Ou, M.S. Strano, R.B. Kaner, A. Mitchell, K. Kalantar-zadeh, Nanostructured tungsten oxide—properties, synthesis, and applications, *Adv. Funct. Mater.* 21 (2011) 2175–2196.
- [23] R. Azimirad, O. Akhavan, A.Z. Moshfegh, Simple method to synthesize Na_xWO_3 nanorods and nanobelts, *J. Phys. Chem. C* 113 (2009) 13098–13102.
- [24] K.B. Lee, S.W. Lee, S. Bin Park, Growth of single-crystalline sodium titanate and sodium tungstate one-dimensional nanostructures: bio-inspired approach using oyster shell, *J. Cryst. Growth* 311 (2009) 4365–4370.
- [25] K.-C. Kim, M.H. Kwak, S.B. Kang, S. Kim, M.-C. Paek, K.-Y. Kang, H.-Y. Kim, J.-H. Jang, C.K. Kim, H.-S. Kye, I.-S. Cheong, Synthesis and characterization of sodium tungsten oxide (Na_xWO_3 , $0 < x < 1$) nanobundles, *Ferroelectrics* 422 (2011) 14–18.
- [26] N.T. Garavand, S.M. Mandavi, A. Irajizad, K. Ahadi, Synthesis of sodium tungsten oxide nano-thick plates, *Mater. Lett.* 82 (2012) 214–216.
- [27] T.T. Xu, J.G. Zheng, N.Q. Wu, A.W. Nicholls, J.R. Roth, D.A. Dikin, R.S. Ruoff, Crystalline boron nanoribbons: synthesis and characterization, *Nano Lett.* 4 (2004) 963–968.
- [28] S.S. Amin, S.-y. Li, J.R. Roth, T.T. Xu, Single crystalline alkaline-earth metal hexaboride one-dimensional (1D) nanostructures: synthesis and characterization, *Chem. Mater.* 21 (2009) 763–770.
- [29] S.S. Amin, S.-y. Li, X. Wu, W. Ding, T.T. Xu, Facile synthesis and tensile behavior of TiO_2 one-dimensional nanostructures, *Nanoscale Res. Lett.* 5 (2010) 338–343.
- [30] H. Zhang, T.T. Xu, M. Tang, T.-h. Her, S.-y. Li, Selective growth of tungsten oxide nanowires via a vapor-solid process, *J. Vac. Sci. Technol. B* 28 (2010) 310–315.
- [31] K. Viswanat, Crystal-structure of sodium tetratungstate, $\text{Na}_2\text{W}_4\text{O}_{13}$, *Dalton Trans.* (1974) 2170–2172.
- [32] V.V. Fomichev, M.E. Poloznikova, O.I. Kondratov, Structural features and spectroscopic and energy characteristics of alkali metal molybdates and tungstates, *Russ. Chem. Rev.* 61 (1992) 877.
- [33] Z.R. Dai, Z.W. Pan, Z.L. Wang, Novel nanostructures of functional oxides synthesized by thermal evaporation, *Adv. Funct. Mater.* 13 (2003) 9–24.
- [34] Data from certificates of analysis provided by vendors.
- [35] J. Zhou, Y. Ding, S.Z. Deng, L. Gong, N.S. Xu, Z.L. Wang, Three-dimensional tungsten oxide nanowire networks, *Adv. Mater.* 17 (2005) 2107.
- [36] K. Hong, M. Xie, H. Wu, Tungsten oxide nanowires synthesized by a catalyst-free method at low temperature, *Nanotechnology* 17 (2006) 4830–4833.
- [37] R.E. Honig, D.A. Kramer, Vapor pressure data for the solid and liquid elements, *RCA Review* 30 (1969) 285–305.